ACS Photonics

Letter

Cite This: ACS Photonics 2019, 6, 1848−1854

pubs.acs.org/journal/apchd5

Titanium Nitride Epitaxial Films as a Plasmonic Material Platform: Alternative to Gold

Wan-Ping Guo,[†] Ragini Mishra,[‡] Chang-Wei Cheng,[§] Bao-Hsien Wu,[∥] Lih-Juann Chen,[∥] Minn-Tsong Lin,[†,⊥] and Shangjr Gwo*[,§,⊥]

[†]Department of Physics, National Taiwan University, Taipei 10617, Taiwan

[‡]Institute of NanoEngineering and MicroSystems, [§]Department of Physics, and [∥]Department of Materials Science and Engineering, National Tsing-Hua University, Hsinchu 30013, Taiwan

[⊥]Research Center for Applied Sciences, Academia Sinica, Taipei 11529, Taiwan

Supporting Information

ABSTRACT: Titanium nitride (TiN) is an interesting refractory metallic compound which could replace gold as an alternative plasmonic material, especially for high temperature and semiconductor compatible applications. However, reported plasmonic properties of TiN films are so far limited by conventional growth techniques, such as reactive sputtering. In this work, we adopt the nitrogen-plasma-assisted molecular-beam epitaxy (MBE) to grow single-crystalline, stoichiometric TiN films on sapphire substrates. The properties of as-grown TiN epitaxial films have been fully characterized by X-ray diffraction (XRD), transmission electron microscopy (TEM), spectroscopic ellipsometry (SE), and surface plasmon polariton (SPP) interferometry. We have confirmed that MBE-grown TiN films exhibit excellent plasmonic properties to replace gold in the visible and near-infrared spectral regions. Measuring the real and imaginary parts of dielectric function by SE, it is also found that TiN is better than gold in the short-wavelength range (<500 nm), where gold suffers from strong loss due to interband transition. Contrary to the recent theoretical prediction that air is not able to stabilize SPP modes at the TiN surface, our surface plasmon interferometry data clearly show the presence of propagating SPP modes at the TiN/air interface. To demonstrate the unique plasmonic properties of MBE-grown stoichiometric TiN, we have fabricated TiN metasurfaces for the visible-spectrum applications.

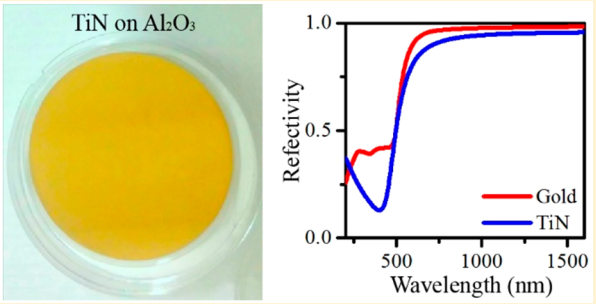

KEYWORDS: *titanium nitride (TiN), gold (Au), plasmonic material, plasmonic metasurface, dielectric function, surface plasmon interferometry, molecular-beam epitaxy*

The rapid developments of plasmonic devices and metasurfaces call for high-performance plasmonic materials.[1−3] Ideal plasmonic materials should possess the properties of low cost, low plasmonic loss, high chemical, mechanical, and thermal stabilities, biocompatibility, spectral tunability, and integrability with present semiconductor technology. Much attention has been given in recent years to plasmonic material alternatives to the conventional noble metals, such as gold and silver. Among the proposed alternative plasmonic materials for gold, titanium nitride (TiN) is an interesting transition-metal compound,[4−8] exhibiting the properties of refractory ceramic (covalent Ti−N bonding) with a high melting temperature (~3000 °C), metallic properties (golden color and high electric conductivity), and a superconductor transition at ~6 K in the case of stoichiometric TiN. Regarding the optical properties, it has recently been shown that TiN is a plasmonic material in the visible and infrared (IR) spectral regions.[4,9−17] Furthermore, TiN possesses extraordinary mechanical strength and durability, high corrosion resistance, as well as excellent complementary metal-oxide-semiconductor (CMOS) and biological compatibilities.[16,18,19] Therefore, TiN-based plasmonics is particularly suitable for biomedical applications,[18,19] CMOS-integrated devices,[16,19] energy harvesting,[20−22] optical devices,[4,13,16] and superconducting quantum devices.[23−26]

In practice, growth of high-quality stoichiometric TiN films requires an ultraclean growth environment because of the propensity of titanium to react with residue gases (e.g., oxygen). It is well-known that titanium is an active absorbing agent and getter material,[7] widely used as a sublimation pump material in ultrahigh vacuum (UHV) systems. Therefore, the achievable material properties of conventional TiN films prepared by sputtering or chemical vapor deposition are limited by the formation of titanium oxynitride and other forms of nonstoichiometric titanium nitride films. It is noticeable that all of the optical properties of TiN films reported in the literature have been measured for the films grown by reactive sputtering,[4,9−13] pulsed laser deposition

Received: April 26, 2019
Published: August 7, 2019

DOI: 10.1021/acsphotonics.9b00617
ACS Photonics 2019, 6, 1848−1854

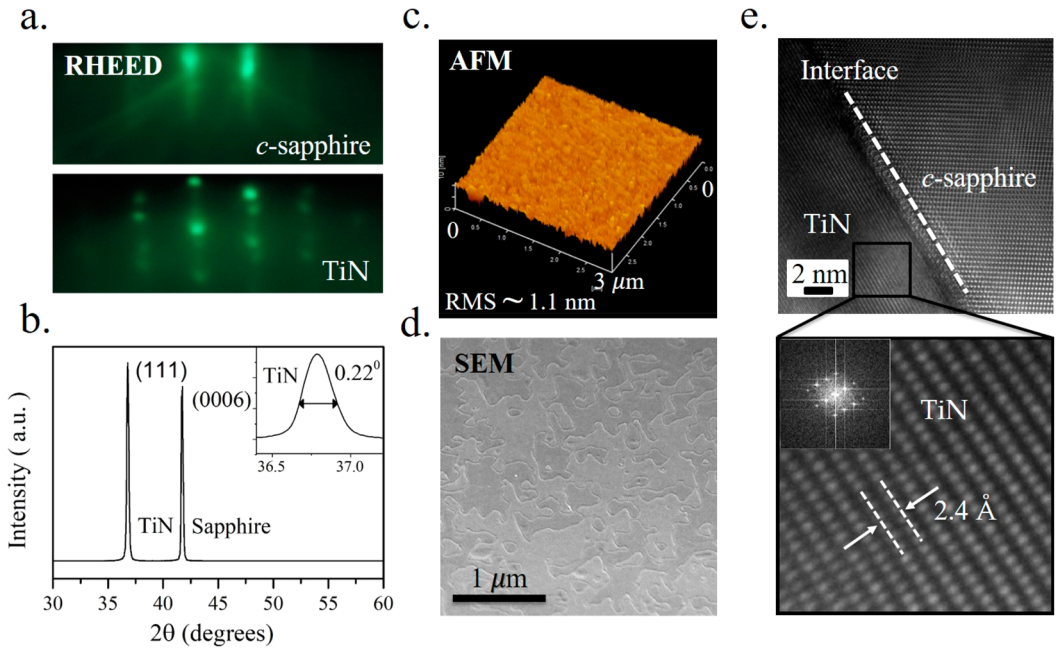

Figure 1. Structural characterization of epitaxial TiN film grown on *c*-sapphire by N_2-plasma-assisted MBE. (a) Reflection high-energy electron diffraction (RHEED) patterns of the *c*-plane sapphire substrate and the epitaxial TiN film before and during MBE growth. (b) X-ray diffraction pattern (X-ray wavelength: 1.54 Å) showing both the close-packed, rock-salt TiN (111) and *c*-plane sapphire (0006) peaks (36.8° and 41.7°). The full width at half-maximum of the TiN (111) and sapphire (0006) peaks are 0.22° and 0.20°, respectively. (c) 3 × 3 μm^2 AFM image taken on the epitaxial TiN film. The root-mean-square (RMS) roughness is about 1.1 nm. (d) SEM image obtained from the TiN epitaxial film, revealing the as-grown surface feature. (e) High-resolution TEM image of the epitaxial TiN film showing clearly the cross-sectional interface region between the TiN epitaxial film and the *c*-sapphire substrate. The lattice parameter between TiN atomic layers along the [111] direction is about 2.4 Å, which is consistent with the TiN lattice parameter (2.44 Å) measured by XRD data , as shown in (b).

(PLD),[14] and atomic layer deposition (ALD).[15,16] Therefore, it remains an important issue regarding the optical properties of stoichiometric TiN films grown by using a UHV growth technique. In this work, we adopt the method of nitrogen (N_2)-plasma-assisted molecular-beam epitaxy (MBE)[25] in a UHV chamber (base pressure ~1×10^{-10} Torr) for the growth of stoichiometric TiN epitaxial films on sapphire substrates.

The crystal structure and surface roughness of MBE-grown TiN films were characterized by X-ray diffraction (XRD), atomic force microscopy (AFM), and scanning electron microscopy (SEM). Moreover, the formation of a single-crystalline, close-packed, rock-salt structure has been confirmed by transmission electron microscopy (TEM). We measured the optical dielectric function of epitaxial TiN films by using spectroscopic ellipsometry (SE). These results show that the structural and optical properties of epitaxial TiN films grown by MBE are consistent with the stoichiometric TiN. To illustrate the potential of TiN-based optical applications for the full visible spectrum, we demonstrate surface plasmon polariton (SPP) interference patterns using a series of double-groove surface interferometer structures with varied groove separations under white-light illumination. Contrary to the recent theoretical prediction that air is not able to stabilize SPP modes at the TiN surface,[17] our surface interferometry results clearly show the presence of propagating SPP modes at the TiN/air interface. Finally, we show the unique optical characteristics of plasmonic metasurfaces based on the epitaxial TiN films, which are better than gold in the short-wavelength region (<500 nm). According to these results, we suggest that the MBE-grown epitaxial TiN films represent a versatile plasmonic material platform in the visible and infrared spectral regions.

In our study, (111)-oriented TiN thin films were grown epitaxial on *c*-plane (0001) sapphire substrates (Figure 1a). XRD characterization reveals that the full width at half-maximum (fwhm) of the main (111) peak is 0.22°, close to the fwhm of sapphire substrate (Figure 1b). The root-mean-square roughness (Figure 1c) and surface morphology (Figure 1d) were measured by AFM and SEM, respectively. The TEM images testify to the high crystalline quality of as-grown TiN films (Figure 1e). The cross-section TEM image demonstrates the formation of an abrupt interface between the TiN film and the sapphire substrate, and a high-resolution TEM image of the TiN region shows that the (111) layer spacing is 2.4 Å, consistent with the XRD data, indicating a close-packed, rock-salt lattice structure, where nitrogen occupies octahedral interstitial sites in the Ti (fcc) sublattice.[17]

Because of the thermodynamic stability in their nitrogen-deficient form, the stoichiometry and carrier concentration of TiN_x films ($x < 1$) can be controlled by the nitrogen plasma flux and sample temperature during the MBE growth. The lower carrier concentration in TiN_x films allows for tunability in their plasmonic response using the electric gating technique.[27] However, we focus here on growing stoichiometric TiN films for optical characterization. Using a Hall effect measurement system, the carrier density (n) is ~9.2×10^{22} cm^{-3}, much higher than the reported values in the literature (Supporting Information, Table S1). Another important indication of forming stoichiometric TiN is the film color, which is very close to the case of gold film.[6] In the Supporting Information, we show some comparison about the optical properties between stoichiometric (TiN) and non-stochiometric (TiN_x) films.

DOI: 10.1021/acsphotonics.9b00617
ACS Photonics 2019, 6, 1848−1854

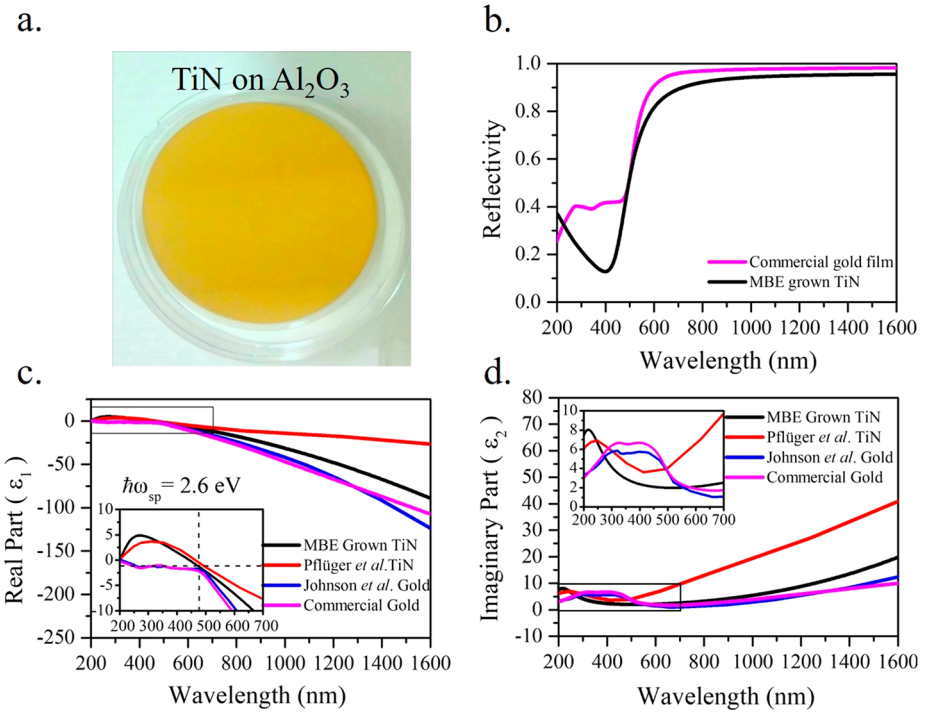

Figure 2. Optical properties of epitaxial TiN film grown on *c*-sapphire. (a) Optical image of an epitaxial TiN film (thickness: 100 nm) grown by MBE on a 2-in., *c*-plane sapphire wafer shows a brilliant golden color, which is a characteristic of stoichiometric TiN film. (b) Calculated optical reflectivity spectrum of the MBE-grown TiN film on *c*-sapphire, in comparison with a commercial gold film (Au(111) on mica) using the spectroscopic ellipsometry (SE) data shown in (c) and (d). (c, d) Dielectric functions (ε_1 and ε_2) measured by SE for a MBE-grown TiN film (our data), a TiN film prepared by sputtering (Pflüger et al.), and a commercial Au(111) film grown on mica. The Johnson and Christy data for gold are also shown for comparison. According to the SE data, the characteristic surface plasmon energy ($\hbar\omega_{sp}$) is 2.6 eV (λ_{sp} = 470 nm, $\varepsilon_1 = -1$) at the TiN/air interface. The value of the imaginary part (ε_2) measured for the MBE-grown TiN film in the 500−700 nm wavelength range is very close to the gold film. By contrast, from 300 to 500 nm, the imaginary part of gold is much larger than TiN because of strong interband transition in gold for light wavelength <500 nm.

In the stoichiometric case, the color of as-grown TiN films (100 nm in thickness) looks very much like gold (Figure 2a). In order to confirm this, we calculated the film reflectivity (see Figure 2b) at normal incidence using the optical dielectric function (i.e., ε_1 and ε_2, the real and imaginary parts of the permittivity $\varepsilon(\omega)$), measured by a spectroscopic ellipsometer, as shown in Figure 2c,d. To determine the dielectric function of 100 nm thick TiN film, we adopted a two-layer structure (air and TiN) by setting TiN as the substrate and the SE data were fitted by using the Drude-Lorentz oscillator model, in which the Drude term stands for the conduction electron contribution, while the Lorentz terms express interband transitions.[14−16]

According to the reflectivity formula $R = \frac{(n-1)^2 + k^2}{(n+1)^2 + k^2}$, where n and k are the real and imaginary parts of the complex refractive index (n and k can be derived from ε_1 and ε_2),[17] the reflectivity of 100 nm thick TiN film is shown to be comparable to a 200 nm thick gold film purchased from PHASIS (Geneva, Switzerland, see Figure 2b), and the reflectivity of the TiN film can be as high as ∼90% when the wavelength is longer than 600 nm. In metal thin-film optics, the imaginary part of permittivity (ε_2) is related to the optical losses. In the visible range (400−700 nm), ε_2 measured for the MBE-grown TiN is very close to the case of gold[28] and much smaller than the case of sputtered TiN films.[9] For the short wavelength region of the visible (400−500 nm), the ε_2 of gold is larger than TiN because of a strong interband transition in gold (see inset in Figure 2d).

For noble metals such as gold, silver, and copper, interband transitions exhibit a step-like threshold behavior. When the incident photon energy is higher than ∼2.5 eV (i.e., wavelength shorter than 500 nm), electron−hole pairs are predominantly excited in gold, instead of surface plasmons. This threshold behavior means that surface plasmon phenomena can be observed only for incident photon energies lower than the interband transition energy. Using the measured dielectric function (Figure 2c), the screening plasmon frequency ω_p (i.e., $\varepsilon_1(\omega_p) = 0$ and the optical reflectivity drop dramatically when $\omega > \omega_p$, as shown in Figure 2b) can be experimentally determined to be $\hbar\omega_p$ = 2.8 eV (λ_p = 442 nm), which is significantly larger than the value reported by the previous experimental studies[9,10] and the recent density functional theory (DFT) calculations at 2.5 eV.[17] In general, when the real part of dielectric function is greater than zero, it is no longer a plasmonic material. Our optical measurement results indicate that the MBE-grown TiN films show very good plasmonic properties. Therefore, not only can we replace TiN for gold in the visible and near-infrared spectral regions, but also TiN outperforms gold in the short-wavelength region (<500 nm).

Next, we explore behavior of surface plasmons propagating at the TiN/air interface. For the case of noble metals (gold and silver), the Drude model formula for the characteristic surface plasma frequency at the metal/air interface can be applied to express $\omega_{sp} = \omega_p/\sqrt{2}$.[29−31] On the other hand, The propagating SPP mode at the interface between metal (ε_m =

DOI: 10.1021/acsphotonics.9b00617
ACS Photonics 2019, 6, 1848−1854

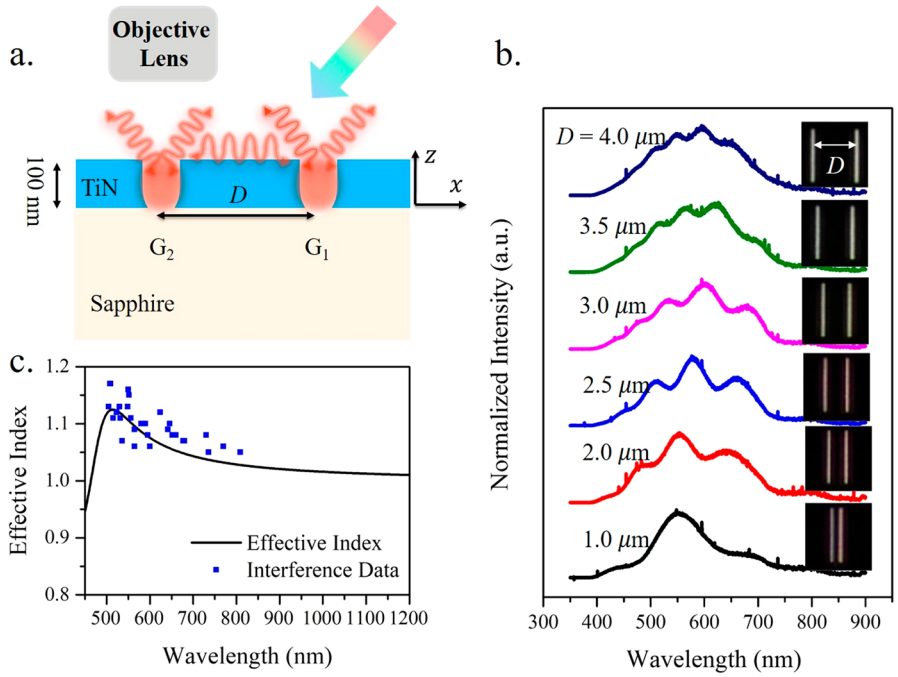

Figure 3. Surface plasmon polariton (SPP) interferometry using TiN surface Fabry-Pérot cavities. (a) Schematic of the white-light interference setup used for measuring the SPP interference patterns from TiN double-nanogroove surface cavities patterned by focused ion beam (FIB) milling with varying nanogroove distances. An oblique incident (75−80°) white light from a halogen lamp was used as the excitation source. (b) SPP interference patterns obtained from different double-nanogroove surface cavities. Corresponding dark-field optical images are shown in the insets. (c) Calculated effectivity index of SPP propagating at the TiN/air interface using the SE data, in comparison to the measured data from TiN nanogroove interference patterns (blue square dots). According to the SPP dispersion equation, the dielectric function of TiN measured by SE is used to determine the effective index ($n_{eff} = \frac{\lambda}{2\pi}\cdot k_r$). The effective index is greater than one when the excitation wave frequency $\omega < \omega_{sp}$ (λ_{sp} = 470 nm), which is consistent with the SE data.

$\varepsilon_1 + i\varepsilon_2$, TiN) and dielectric ($\varepsilon_d$ = 1, air) is possible when the SPP wavevector k_{spp} satisfies the dispersion equation, $k_{spp} = \frac{\omega}{c}\mathrm{Re}\left(\sqrt{\frac{\varepsilon_m\varepsilon_d}{\varepsilon_m+\varepsilon_d}}\right)$, where $k_0 = \frac{\omega}{c}$ is the free-space wavevector.[29−31] In Figure 2c, we can experimentally determine $\hbar\omega_p$ = 2.6 eV by locating the frequency satisfying $\varepsilon_1(\omega_{sp}) = -1$, which arrives at 2.6 eV (λ_{sp} = 470 nm), which is very close to the previous experimental data of 2.67 eV[14] and larger than the DFT calculation value at 2.48 eV.[17] When $\omega < \omega_{sp}$, bound SPPs propagates at the metal/air interface with a wavevector larger than light in the dielectric at the same energy. While, when $\omega > \omega_p$, the metal becomes transparent to the incoming photons and we have the radiative mode, where the excited wave is no longer confined at the interface.

In a recent theoretical study by Catellani and Calzolari,[17] it is predicted that SPPs cannot be stabilized at the TiN/air interface because the SPP dispersion is too close to the light line, resulting in a radiative mode at low k_{spp}. However, the experimental dispersion determined by us shows better plasmonic properties (both ε_1 and ε_2) to allow confined SPP modes at the TiN/air interface. There is a very simple and straight method to measure propagating SPP modes at the metal/dielectric by observing surface plasmon interference patterns on patterned metal surface with surface interferometer structures, which also can be used to compare with the measured metal dielectric function in the full visible range.[32−35] Here, we show that clear SPPs interference patterns can be obtained on high-quality single-crystalline TiN films using a focused ion beam (FIB)-milled double-nanogroove structure on the TiN surface (Figure 3a). In principle, the interference fringe pattern can be varied by varying the nanogroove separation.[32,35] Therefore, we designed nanogroove pairs with different separations (D = 1.0−4.0 μm) at fixed groove length (6 μm), width (80 nm), and depth (70 nm), and SPPs were excited by using a halogen white-light source with an incident angle around 75−80°. The interference fringes originated from propagating SPPs clearly appear when the nanogroove separation is varied from 1.0 to 4.0 μm (Figure 3b). Benefiting from the low-loss film properties (long SPP propagating length), the propagating SPP waves can be reflected back and forth between two nanogrooves (even for the case of 4.0 μm separation) before decoupling at nanogrooves into the far-field radiation (photons) for optical measurement. The scattering (decoupled) photons were collected from the nanogroove G_2, as shown in Figure 3a, through an objective lens (100×, N.A. = 0.8), and Fabry-Pérot interference patterns were recorded by using an optical spectrometer The scattering intensity from the nanogroove is decided by $Ee^{i(x\cdot k_{spp})}$, in which E is the amplitude and k_{spp} is the SPP wavenumber. The peak and dips position of SPP interference can be extracted from different nanogroove interference patterns to be compared with the dielectric function measured by SE. The relationship between real part of SPPs wave vector (k_r) and interferences peaks and dips satisfy the following equations:[32,35]

$$\text{dips:}\quad 2k_rD = 2l\pi \quad (l = 0, 1, 2, \ldots) \tag{1}$$

$$\text{peaks:}\quad 2k_rD = (2l+1)\pi \quad (l = 0, 1, 2, \ldots) \tag{2}$$

DOI: 10.1021/acsphotonics.9b00617
ACS Photonics 2019, 6, 1848−1854

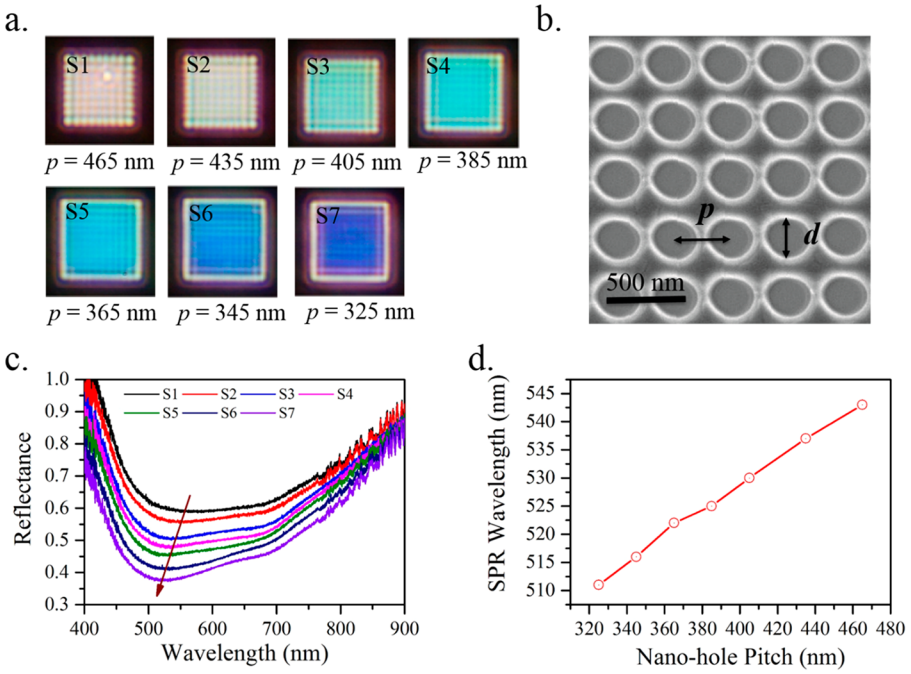

Figure 4. Optical properties TiN metasurfaces with varying structural parameters. (a) Dark-field optical images of TiN metasurfaces composed of nanohole arrays. The nanohole diameter is fixed at 256 nm and the pitch is varied from 465 to 325 nm. (b) SEM image of the TiN metasurface with diameter d = 256 nm and pitch p = 325 nm. The corresponding reflectance spectrum is shown in (c). (c) Reflectance spectra corresponding to TiN nanohole arrays with different pitches. The bare, unpatterned TiN film is used as the reference for reflectance measurement. (d) The measured collective surface plasmon resonance (CSPR) wavelengths blue shift with decreasing nanohole pitch.

where k_r is the real part of the SPP wavenumber. After extracting the $k_r(\lambda)$ and substituting it into the equation, $n_{eff} = \frac{\lambda}{2\pi}\cdot k_r$, the wavelength-dependent effective index (n_{eff}) can then be experimentally determined. On the other hand, the SPP dispersion relation can be obtained by using the dielectric function and the following expression:

$$k_{spp} = k_0\sqrt{\frac{\varepsilon_d\varepsilon_m}{\varepsilon_d + \varepsilon_m}} \tag{3}$$

where k_{spp}=k_r+ik_i is a complex value, $k_0 = \frac{\omega}{c}$ is the free-space wavevector, ε_d and ε_m stand for frequency-dependent permittivities of the metal ($\varepsilon_m(\omega)$) and the dielectric (ε_d = 1 for air), respectively. So, we can use eq 3 to calculate the frequency-dependent SPP wavenumber and effective indices for SPPs propagating at the TiN and air interface (Figure 3c). Both approaches converge to the same effective index curve, in particular, when the excited frequency $\omega < \omega_{sp}$ (λ_{sp} = 470 nm) and the effective index $n_{eff} > 1$. These results indicate that MBE-grown single-crystalline TiN films can sustain long-distance SPP propagation at the metal−air interface.

Finally, we show that plasmonic color generation can be realized by using subwavelength TiN metasurfaces. The plasmonic resonance of metal nanostructures is well-known to allow the manipulation of light-matter interactions beyond the diffraction limit.[36,37] In the plasmonic resonant bands, the incident light can be resonantly absorbed or scattered by plasmonic nanostructures, and these resonances can be controlled precisely with the geometry and size of plasmonic nanostructures (localized surface plasmon resonance, LSPR), as well as their pitch in the surface plasmonic nanostructure array (collective surface plasmon resonance, CSPR).[38−40] This phenomenon has been used as the foundation to design a myriad of plasmonic color generation schemes, including transmission filters,[41] reflective color printing,[42,43] and surface holograms.[44] So far, the reported work about plasmonic color generation has been focused on silver and aluminum plasmonic structures, which can generate colors in the full visible range.[41−43] In the present demonstration, subwavelength nanoholes were milled into TiN films by FIB to generate plasmonic colors using the refractory TiN plasmonic material platform. Compared to gold for plasmonic color generation, which has a low-bound wavelength limitation at 500 nm, TiN can sustain a broader visible range (Figure 4a). Moreover, the high melting temperature and chemical stability of TiN can extend plasmonic color printing beyond silver and aluminum for more practical device applications in harsh environments.

To demonstrate the broadband tunability of the CSPR band, resulting from coupling of closely spaced plasmonic nanostructures arranged in a surface array, we milled nanoholes into TiN films by FIB with different pitches (p) and kept the diameter of nanoholes fixed at d = 256 nm (Figure 4b). Under different pitches, which were varied from 465 to 325 nm, we can observe a broad CSPR spectral response over the visible range in the dark-field optical microscopy images (Figure 4a). Due to the far-field dipole−dipole interaction in the close-packed nanoholes array, we can observe a pronounced blue shift of the CSPR band with decreasing nanohole pitch (Figure 4c,d),[38] while under near-field coupling, we should observe a red shift with an exponential dependence on the gap distance between neighboring nanoholes.[39] In Figure 4c, the observed decrease of reflectance (a pristine TiN film is used as reference) with increasing pitch in the nanohole array is due to the change in the surface density of nanoholes, as well as the pitch dependence of objective lens coupling (in- and out-coupling) efficiency in dark-field optical microscopy.[40] The reflectance spectra presented here indicate that the TiN

DOI: 10.1021/acsphotonics.9b00617
ACS Photonics 2019, 6, 1848−1854

nanohole metasurface can have a broad and engineerable spectral response based on their structural parameters. Therefore, this approach offers the potential to design resonant optical devices in the visible range, which are compatible with the CMOS process.

In summary, stoichiometric TiN epitaxial films grown on sapphire substrates possess excellent mechanical, chemical, and optical properties to be used as an alternative plasmonic material of gold in the visible and near-infrared spectral regions. We have confirmed that stoichiometric TiN is better than gold in the short-wavelength range (<500 nm) and air is able to stabilize SPP modes at the TiN surface. Both have important implications for optical applications based on TiN plasmonic metasurfaces. Our surface plasmon interferometry results clearly show the presence of propagating SPP modes at the TiN/air interface. Taking advantage of their other superior materials properties, other application areas including solar energy harvesting, metasurface-based nonlinear optics, biocompatible sensing, nanoelectromechanical systems, and superconducting quantum devices can also be expected.

EXPERIMENTAL METHODS

Epitaxial-Grown, Single-Crystal Titanium Nitride. Single-crystal titanium nitride films were grown by a nitrogen-plasma-assisted molecular-beam epitaxy system (DCA Instruments Oy, Turku, Finland) on 2-in., *c*-plane (0001) sapphire substrates. The MBE base pressure was kept about 1×10^{-10} Torr before growth. Commercial double-side-polished sapphire wafers are used as substrates, which were first thermally cleaned at 800 °C for 1 h. Then, we raised the substrate temperature to 1000 °C and holding it for about 30 min. While keeping the substrate temperature at 1000 °C, nitridation of the *c*-plane sapphire substrate was performed for a few minutes using a nitrogen plasma source (Veeco Instruments, U.S.A.). The Ti flux was supplied by a high-temperature Knudsen cell and the TiN deposition rate is about 2 nm/min. During titanium nitride growth, an in situ reflection high-energy electron diffraction pattern revealed that single-crystalline TiN has been grown.

Dielectric Function Measurements. The permittivity of TiN films was measured by using spectroscopic ellipsometer (m2000, J. A. Woollam Co., U.S.A.), which was supported by the National Nano Device Laboratories (NDL) in Taiwan.

Electronic Characteristic. The electronic characteristics, such as carrier density and mobility, was obtained by using a Hall effect measurement system.

Energy-Dispersive X-ray Spectroscopy. The chemical stoichiometry ratios of TiN films were confirmed by using an energy-dispersive spectrometer (EDS) installed in a Helios Nanolab 600i DualBeam system (FEI, U.S.A.). The scan area is 5×5 μm^2 at a 15 kV acceleration voltage.

Nanostructure Fabrication. All of the nanogroove and nanohole structures on the TiN single-crystalline films were fabricated by using a FIB system (FEI Helios Nanolab 600i). These structures were milled at a 30 kV acceleration voltage and an ion beam current of 7.7 pA.

ASSOCIATED CONTENT

Supporting Information

The Supporting Information is available free of charge on the ACS Publications website at DOI: 10.1021/acsphotonics.9b00617.

TEM and SEM images of the stoichiometric TiN epitaxial film and the groove milled by FIB for surface plasmon interferometry measurement, comparison of optical properties (optical images, reflectivity spectra, and dielectric functions) for Au, TiN, $TiN_{0.28}$, and Ti films, table of electrical characteristics of TiN films from literature results and our data, and the complete dielectric function measured by SE for the stoichiometric TiN epitaxial film (PDF)

AUTHOR INFORMATION

Corresponding Author

*E-mail: gwo@phys.nthu.edu.tw.

ORCID

Lih-Juann Chen: 0000-0002-0826-8680

Shangjr Gwo: 0000-0002-3013-0477

Notes

The authors declare no competing financial interest.

ACKNOWLEDGMENTS

Spectroscopic ellipsometry (SE) measurements were performed at the National Nano Device Laboratories (NDL) in Hsinchu, Taiwan. FIB nanofabrication was performed at the Center for Nanotechnology, Materials Science and Microsystems, National Tsing-Hua University. We would like to acknowledge the funding support from the Ministry of Science and Technology in Taiwan for this research work (MOS-108-2119-M-007-008, MOST-105-2112-M-007-011-MY3, MOST-107-2923-M-007-004-MY3, MOST-107-2119-M-002-006).

REFERENCES

(1) West, P. R.; Ishii, S.; Naik, G. V.; Emani, N. K.; Shalaev, V. M.; Boltasseva, A. Searching for better plasmonic materials. *Laser Photonics Rev.* **2010**, *4*, 795−808.

(2) Boltasseva, A.; Atwater, H. A. Low-Loss Plasmonic Metamaterials. *Science* **2011**, *331*, 290−291.

(3) Dastmalchi, B.; Tassin, P.; Koschny, T.; Soukoulis, C. A new perspective on plasmonics: confinement and propagation length of surface plasmons for different materials and geometries. *Adv. Opt. Mater.* **2016**, *4*, 177−184.

(4) Naik, G. V.; Schroeder, J. L.; Ni, X.; Kildishev, A. V.; Sands, T. D.; Boltasseva, A. Titanium nitride as a plasmonic material for visible and near-infrared wavelengths. *Opt. Mater. Express* **2012**, *2*, 478−489.

(5) Guler, U.; Boltasseva, A.; Shalaev, V. M. Refractory plasmonics. *Science* **2014**, *344*, 263−264.

(6) Boltasseva, A.; Shalaev, V. M. All that glitters need not be gold. *Science* **2015**, *347*, 1308−1310.

(7) Igasaki, Y.; Mitsuhashi, H.; Azuma, K.; Muto, T. Structure and electrical properties of titanium nitride films. *Jpn. J. Appl. Phys.* **1978**, *17*, 85−96.

(8) Spengler, W.; Kaiser, R.; Christensen, A. N.; Müller-Vogt, G. Raman scattering, superconductivity, and phonon density of states of stoichiometric and nonstoichiometric TiN. *Phys. Rev. B: Condens. Matter Mater. Phys.* **1978**, *17*, 1095−1101.

(9) Pflüger, J.; Fink, J.; Weber, W.; Bohnen, K. P.; Crecelius, G. Dielectric properties of TiC_x, TiN_x, VC_x, and VN_x from 1.5 to 40 eV determined by electron-energy-loss spectroscopy. *Phys. Rev. B: Condens. Matter Mater. Phys.* **1984**, *30*, 1155−1163.

(10) Patsalas, P.; Logothetidis, S. Optical, electronic, and transport properties of nanocrystalline titanium nitride thin films. *J. Appl. Phys.* **2001**, *90*, 4725−4734.

(11) Chen, N. C.; Lien, W. C.; Liu, C. R.; Huang, Y. L.; Lin, Y. R.; Chou, C.; Chang, S. Y.; Ho, C. W. Excitation of surface plasma wave at TiN/air interface in the Kretschmann geometry. *J. Appl. Phys.* **2011**, *109*, 043104.

DOI: 10.1021/acsphotonics.9b00617
ACS Photonics 2019, 6, 1848−1854

(12) Naik, G. V.; Saha, B.; Liu, J.; Saber, S. M.; Stach, E. A.; Irudayaraj, J. M. K.; Sands, T. D.; Shalaev, V. M.; Boltasseva, A. Epitaxial superlattices with titanium nitride as a plasmonic component for optical hyperbolic metamaterials. *Proc. Natl. Acad. Sci. U. S. A.* **2014**, *111*, 7546−7551.
(13) Shah, D.; Reddy, H.; Kinsey, N.; Shalaev, V. M.; Boltasseva, A. Optical properties of plasmonic ultrathin TiN films. *Adv. Opt. Mater.* **2017**, *5*, 1700065.
(14) Murai, S.; Fujita, K.; Daido, Y.; Yasuhara, R.; Kamakura, R.; Tanaka, K. Plasmonic arrays of titanium nitride nanoparticles fabricated from epitaxial thin films. *Opt. Express* **2016**, *24*, 1143−1153.
(15) Langereis, E.; Heil, S. B. S.; van de Sanden, M. C. M.; Kessels, W. M. M. *In situ* spectroscopic ellipsometry study on the growth of ultrathin TiN films by plasma-assisted atomic layer deposition. *J. Appl. Phys.* **2006**, *100*, 023534.
(16) Briggs, J. A.; Naik, G. V.; Petach, T. A.; Baum, B. K.; Goldhaber-Gordon, D.; Dionne, J. A. Fully CMOS-compatible titanium nitride nanoantennas. *Appl. Phys. Lett.* **2016**, *108*, 051110.
(17) Catellani, A.; Calzolari, A. Plasmonic properties of refractory titanium nitride. *Phys. Rev. B: Condens. Matter Mater. Phys.* **2017**, *95*, 115145.
(18) He, W.; Ai, K.; Jiang, C.; Li, Y.; Song, X.; Lu, L. Plasmonic titanium nitride nanoparticles for in vivo photoacoustic tomography imaging and photothermal cancer therapy. *Biomaterials* **2017**, *132*, 37−47.
(19) Birkholz, M.; Ehwald, K. E.; Kulse, P.; Drews, J.; Fröhlich, M.; Haak, U.; Kaynak, M.; Matthus, E.; Schulz, K.; Wolansky, D. Ultrathin TiN Membranes as a Technology Platform for CMOS-Integrated MEMS and BioMEMS Devices. *Adv. Funct. Mater.* **2011**, *21*, 1652−1656.
(20) Kraemer, D.; Poudel, B.; Feng, H.-P.; Caylor, J. C.; Yu, B.; Yan, X.; Ma, Y.; Wang, X.; Wang, D.; Muto, A.; McEnaney, K.; Chiesa, M.; Ren, Z.; Chen, G. High-performance flat-panel solar thermoelectric generators with high thermal concentration. *Nat. Mater.* **2011**, *10*, 532−538.
(21) Fan, S. Photovoltaics: An alternative 'Sun' for solar cells. *Nat. Nanotechnol.* **2014**, *9*, 92−93.
(22) Naldoni, A.; Guler, U.; Wang, Z.; Marelli, M.; Malara, F.; Meng, X.; Besteiro, L. V.; Govorov, A. O.; Kildishev, A. V.; Boltasseva, A.; Shalaev, V. M. Broadband hot-electron collection for solar water splitting with plasmonic titanium nitride. *Adv. Opt. Mater.* **2017**, *5*, 1601031.
(23) Ohya, S.; Chiaro, B.; Megrant, A.; Neill, C.; Barends, R.; Chen, Y.; Kelly, J.; Low, D.; Mutus, J.; O'Malley, P. J. J.; Roushan, P.; Sank, D.; Vainsencher, A.; Wenner, J.; White, T. C.; Yin, Y.; Schultz, B. D.; Palmstrøm, C. J.; Mazin, B. A.; Cleland, A. N.; Martinis, J. M. Room temperature deposition of sputtered TiN films for superconducting coplanar waveguide resonators. *Supercond. Sci. Technol.* **2014**, *27*, 015009.
(24) Jaim, H. M. I.; Aguilar, J. A.; Sarabi, B.; Rosen, Y. J.; Ramanayaka, A. N.; Lock, E. H.; Richardson, C. J. K.; Osborn, K. D. Superconducting tin films sputtered over a large range of substrate dc bias. *IEEE Trans. Appl. Supercond.* **2015**, *25*, 1100505.
(25) Olson, G. A. Growth of titanium nitride thin films for low-loss superconducting quantum circuits. *Ph.D. thesis*, The University of Illinois at Urbana-Champaign, 2015.
(26) Zhu, D.; Zhao, Q.-Y.; Choi, H.; Lu, T.-J.; Dane, A. E.; Englund, D.; Berggren, K. K. A Scalable multi-photon coincidence detector based on superconducting nanowires. *Nat. Nanotechnol.* **2018**, *13*, 596−601.
(27) Lu, Y.-J.; Sokhoyan, R.; Cheng, W.-H.; Shirmanesh, G. K.; Davoyan, A. R.; Pala, R. A.; Thyagarajan, K.; Atwater, H. A. Dynamically controlled Purcell enhancement of visible spontaneous emission in a gated plasmonic heterostructure. *Nat. Commun.* **2017**, *8*, 1631.
(28) Johnson, P. B.; Christy, R. W. Optical constants of the noble metals. *Phys. Rev. B* **1972**, *6*, 4370−4379.
(29) Sambles, J. R.; Bradbery, G. W.; Yang, F. Optical excitation of surface plasmons: an introduction. *Contemp. Phys.* **1991**, *32*, 173−183.
(30) Maier, S. A. *Plasmonics: Fundamentals and Applications*; Springer: New York, 2007.
(31) Dionne, J. A.; Sweatlock, L. A.; Atwater, H. A.; Polman, A. Planar metal plasmon waveguides: frequency-dependent dispersion, propagation, localization, and loss beyond the free electron model. *Phys. Rev. B: Condens. Matter Mater. Phys.* **2005**, *72*, 075405.
(32) Wang, C. Y.; Chen, H.-Y.; Sun, L.; Chen, W.-L.; Chang, Y.-M.; Ahn, H.; Li, X.; Gwo, S. Giant colloidal silver crystals for low-loss linear and nonlinear plasmonics. *Nat. Commun.* **2015**, *6*, 7734.
(33) Ditlbacher, H.; Hohenau, A.; Wagner, D.; Kreibig, U.; Rogers, M.; Hofer, F.; Aussenegg, F. R.; Krenn, J. R. Silver nanowires as surface plasmon resonators. *Phys. Rev. Lett.* **2005**, *95*, 257403.
(34) Temnov, V. V.; Woggon, U.; Dintinger, J.; Devaux, E.; Ebbesen, T. W. Surface plasmon interferometry: measuring group velocity of surface plasmons. *Opt. Lett.* **2007**, *32*, 1235−1237.
(35) Cheng, C.-W.; Liao, Y.-J.; Liu, C.-Y.; Wu, B.-H.; Raja, S. S.; Wang, C.-Y.; Li, X.; Shih, C.-K.; Chen, L.-J.; Gwo, S. Epitaxial aluminum-on-sapphire films as a plasmonic material platform for ultraviolet and full visible spectral regions. *ACS Photonics* **2018**, *5*, 2624−2630.
(36) Ebbesen, T. W.; Lezec, H. J.; Ghaemi, H. F.; Thio, T.; Wolff, P. A. Extraordinary optical transmission through sub-wavelength hole arrays. *Nature* **1998**, *391*, 667−669.
(37) Ghaemi, H. F.; Thio, T.; Grupp, D. E.; Ebbesen, T. W.; Lezec, H. J. Surface plasmons enhance optical transmission through subwavelength holes. *Phys. Rev. B: Condens. Matter Mater. Phys.* **1998**, *58*, 6779−6782.
(38) Lamprecht, B.; Schider, G.; Lechner, R. T.; Ditlbacher, H.; Krenn, J. R.; Leitner, A.; Aussenegg, F. R. Metal nanoparticle gratings: influence of dipolar particle interaction on plasmon resonance. *Phys. Rev. Lett.* **2000**, *84*, 4721−4724.
(39) Chen, C.-F.; Tzeng, S.-D.; Chen, H.-Y.; Lin, K.-J.; Gwo, S. Tunable plasmonic response from alkanethiolate-stabilized gold nanoparticle superlattices: evidence of near field coupling. *J. Am. Chem. Soc.* **2008**, *130*, 824−826.
(40) Liu, H.-W.; Lin, F.-C.; Lin, S.-W.; Wu, J.-Y.; Chou, B.-T.; Lai, K.-J.; Lin, S.-D.; Huang, J.-S. Single-crystalline aluminum nanostructures on a semiconducting GaAs substrate for ultraviolet to near-infrared plasmonics. *ACS Nano* **2015**, *9*, 3875−3886.
(41) Yokogawa, S.; Burgos, S. P.; Atwater, H. A. Plasmonic color filters for CMOS image sensor applications. *Nano Lett.* **2012**, *12*, 4349−4354.
(42) Kumar, K.; Duan, H.; Hegde, R. S.; Koh, S. C. W.; Wei, J. N.; Yang, J. K. W. Printing colour at the optical diffraction limit. *Nat. Nanotechnol.* **2012**, *7*, 557−561.
(43) Tan, S. J.; Zhang, L.; Zhu, D.; Goh, X. M.; Wang, Y. M.; Kumar, K.; Qiu, C.-W.; Yang, J. K. W. Plasmonic color palettes for photorealistic printing with aluminum nanostructures. *Nano Lett.* **2014**, *14*, 4023−4029.
(44) Huang, Y.-W.; Chen, W. T.; Tsai, W.-Y.; Wu, P. C.; Wang, C.-M.; Sun, G.; Tsai, D. P. High-efficiency broadband meta-hologram with polarization-controlled dual images. *Nano Lett.* **2015**, *15*, 3122−3127.

DOI: 10.1021/acsphotonics.9b00617
ACS Photonics 2019, 6, 1848−1854